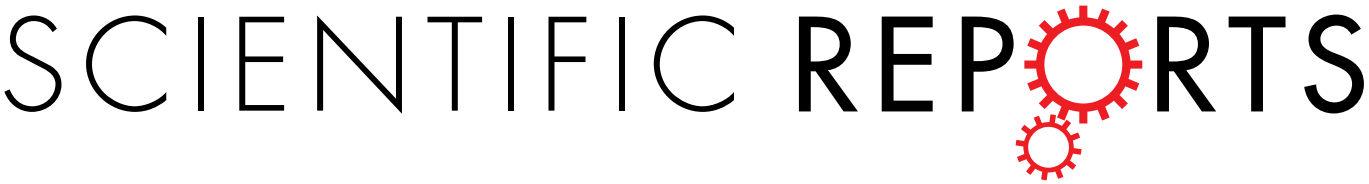

OPEN

Development of Highly Active Bifunctional Electrocatalyst Using Co_3O_4 on Carbon Nanotubes for Oxygen Reduction and Oxygen Evolution

Received: 11 September 2017
Accepted: 26 January 2018
Published online: 07 February 2018

Mohammad Shamsuddin Ahmed, Byungchul Choi & Young-Bae Kim

Replacement of precious platinum catalyst with efficient and cheap bifunctional alternatives would be significantly beneficial for electrocatalytic oxygen reduction reaction (ORR) and oxygen evolution reaction (OER) and the application of these catalysts in fuel cells is highly crucial. Despite numerous studies on electrocatalysts, the development of bifunctional electrocatalysts with comparatively better activity and low cost remains a big challenge. In this paper, we report a nanomaterial consisting of nanocactus-shaped Co_3O_4 grown on carbon nanotubes (Co_3O_4/CNTs) and employed as a bifunctional electrocatalyst for the simultaneous catalysis on ORR, and OER. The Co_3O_4/CNTs exhibit superior catalytic activity toward ORR and OER with the smallest potential difference (0.72 V) between the $E_{j_{10}}$ (1.55 V) for OER and $E_{1/2}$ (0.83 V) for ORR. Thus, Co_3O_4/CNTs are promising high-performance and cost-effective bifunctional catalysts for ORR and OER because of their overall superior catalytic activity and stability compared with 20 wt% Pt/C and RuO_2, respectively. The superior catalytic activity arises from the unique nanocactus-like structure of Co_3O_4 and the synergetic effects of Co_3O_4 and CNTs.

Fabrication of hybrid nanomaterials that preserves improved properties other than the original properties of their base materials is an important issue in nanoscience and technology. Among the different allotropes of carbon nanomaterials, carbon nanotubes (CNTs) are one of the most promising nanomaterials for catalysis and sensing[1–4]. The catalytic sites in renewable and green energy systems need to be supported on conducting materials. These sites can be made of metallic nanostructures (such as nanoparticles and nanoflowers) or organometallic complexes. CNTs are potential ideal support material for electrocatalysts because of its electrical conductivity, high surface area, and relatively enhanced durability[5]. Noncovalent chemical approach to ensure a close incorporation between the CNTs and the metallic sites is promising because of its simple fabrication method and better preservation of the electronic properties of the CNTs without damaging the π-configuration.

Persistent environmental impact and increasing demands of traditional energy resources, such as, oil, gas, and coal have stimulated extensive efforts worldwide to develop renewable and green energy technologies, such as fuel cells (FCs) and water splitting systems[1,6–12]. Among many electrochemical reactions in FCs, the oxygen reduction reaction (ORR) is considered as the heart of FCs because it is the only reaction in cathode. By contrast, electrocatalytic oxygen evolution reaction (OER) through water splitting has been recognized as one of the most promising ways to generate oxygen[4]. Precious metals such as platinum (Pt) and/or its alloy materials have been most frequently used active electrocatalyst for both reactions[13–16]. However, Pt-based materials are susceptible to the poor durability and crossover effect in FCs[17,18]. Moreover, the high cost and bottleneck reserve in nature of Pt have also prohibited the full commercialization of FCs[19,20]. Meanwhile, transition metals and their alloys[21–24] have been demonstrated as promising catalysts for ORR and/or OER. So far, the catalytic activities of many nonprecious metal electrocatalysts remain too low compared with those of noble metal catalysts. Moreover, the catalytic activity of the former electocatalysts is largely hindered by their inherent corrosion and oxidation susceptibility.

Department of Mechanical Engineering, Chonnam National University, Gwangju, Republic of Korea. Correspondence and requests for materials should be addressed to Y.-B.K. (email: ybkim@chonnam.ac.kr)

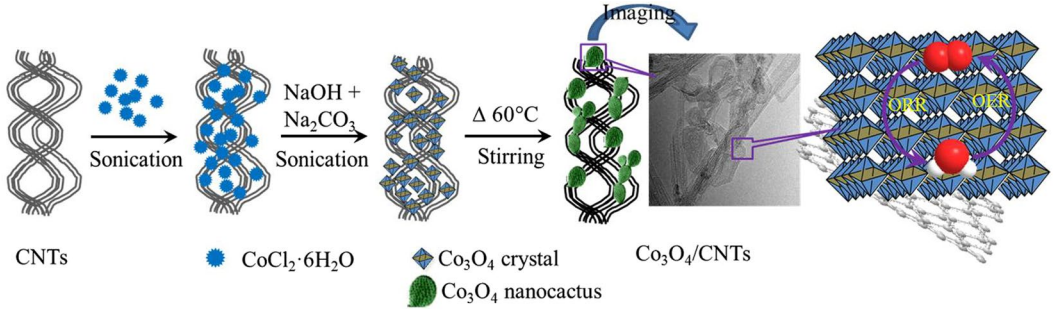

Figure 1. The schematic diagram of Co_3O_4/CNTs preparation and its catalytic activity.

A number of cobalt oxides with uniform porous structure and large surface area have been employed as non-precious catalysts to the electrochemical energy conversion reactions[25–29]. These catalysts have currently attracted much interest in the field of electrocatalysis because of their chemical and physical properties[29]. In particular, Co_3O_4 with spinel crystal structure is beneficial for the electron transport between Co^{2+} and Co^{3+} ions. Thus, Co_3O_4 has been widely considered as an efficient electrocatalyst for ORR and OER[30–33]. However, Co_3O_4 itself shows lower electrocatalytic activity because of its low electrical conductivity and dissolution, short active site density and agglomeration nature during electrocatalytic processes[30]. Nevertheless, further studies have exhibited that the synergy between carbon nanomaterials (i.e. graphene and CNTs) and Co_3O_4 can give a huge promotion of the electrocatalytic activity[26,28,34–37]. Many researches have investigated on Co_3O_4-based hybrid catalysts and obtained uniformly dispersed Co_3O_4 nanostructures (i.e. nanoparticles, core-shell, and hollow sphere) to improve electrocatalyst activity[30,38–41]. The results show that the size and shape of the nanocatalysts are deeply related to their electrocatalytic performances, and using these hybrid catalysts is considered one of the best strategies for improving catalytic activity and stability[42].

Multifunctional (i.e. bifunctional or trifunctional)[28,41,43] catalyst systems have been reported. However, a bifunctional catalyst system with enhanced activity for ORR and OER is difficult to develop because of the pH-dependent activity and stability[43]. OER electrocatalysts exhibit poor performance in alkaline electrolyte than acid electrolyte[44]. So far, doped-free and noncovalent CNTs with Co_3O_4-hybrid bifunctional catalyst for ORR, and OER has not been reported to date, although the N-doped graphene or CNTs with Co_3O_4-hybrid catalysts are rarely discussed[28,30]. Therefore, new strategies to develop a simply prepared, highly efficient, and cost-effective Co_3O_4- and CNT-based hybrid bifunctional electrocatalysts for ORR and OER is desirable for the large-scale production of clean energy. In this study, we have developed a simple strategy to synthesize Co_3O_4 nanocactus grown on CNTs (Co_3O_4/CNTs; in Fig. 1). For the first time, the Co_3O_4/CNTs were successfully employed as bifunctional Co_3O_4-based electrocatalyst for ORR and OER. The porous Co_3O_4/CNTs exhibited superior electrocatalytic activity and stability than the benchmarks Pt/C or RuO_2 for ORR and OER, respectively, because of their high density of active sites and excellent charge transport capability.

Experimental Section

The Co_3O_4/CNTs were synthesized by a simple chemical method. In a typical preparation, $CoCl_2.6H_2O$ (62 mg) was mixed with 30 mL of water. Then, 30 mg of multiwalled CNTs, which were treated with acid for 30 min[45], were mixed with 30 mL of water. The solution was added into the $CoCl_2.6H_2O$ solution and vigorously stirred for 1 h. The pH was controlled by slowly adding a solution of 0.21 mol L^{-1} NaOH and 0.066 mol L^{-1} Na_2CO_3 under vigorous stirring until pH 10 was reached at room temperature (RT). The prepared suspension was kept at 60 °C for next 24 h under gentle stirring. Finally, the Co_3O_4/CNTs were filtered and washed with water for and dried at 60 °C. The bare CNTs were prepared using the same protocol but without addition of $CoCl_2.6H_2O$ solution. Also, the Co_3O_4/CNTs in various pH values (i.e. pH 7, 12, 14) were prepared by controlled addition of aforementioned alkaline solution. The electrochemical and instrumental characterizations were described in the supporting information.

Results and Discussions

Figure 1 shows that the Co_3O_4 precursor and clean CNTs were mixed with a simple cooperative assembly of prepared alkaline solution in water at RT. The solution was then kept at 60 °C under gentle stirring for next 24 h to form Co_3O_4 nanocactus onto CNTs. The growth of Co_3O_4 nanocactus probably goes through a modified mechanism as below[46]-

$$NaOH + Na_2CO_3 \rightarrow 3Na^+ + OH^- + CO_3^{2-} \quad (1)$$

$$CoCl_2 \rightarrow Co^{2+} + 2Cl^- \quad (2)$$

$$Co^{2+} + 2Cl^- + 2Na^+ + 2OH^- \rightarrow Co(OH)_2 + 2NaCl \quad (3)$$

$$4Co(OH)_2 + 2CO_3^{2-} + OH^- \rightarrow 4CoOOH + 2CO_2\uparrow + 2H_2O \quad (4)$$

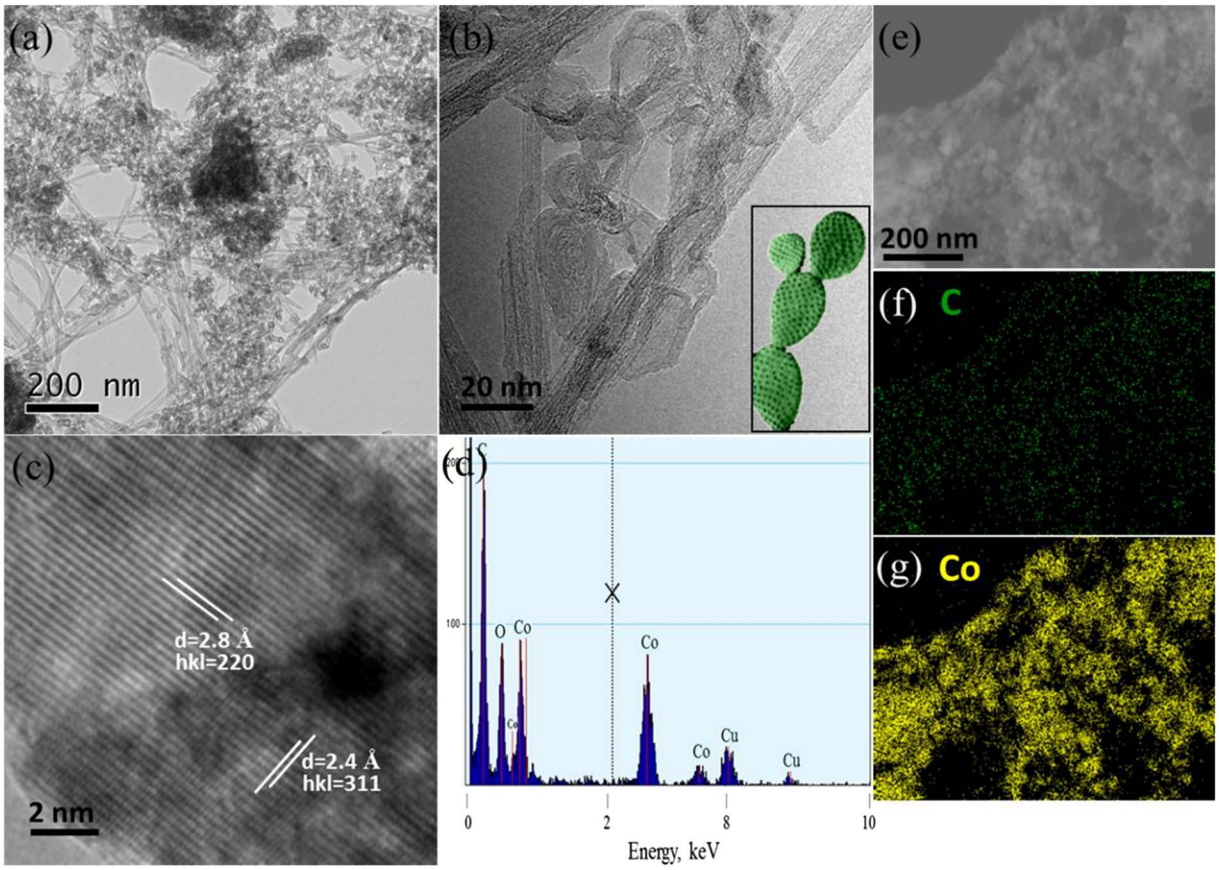

Figure 2. TEM (**a** and **b**), HRTEM (**c**) images, EDX spectrum (**d**), bright-fiend TEM image (**e**) and C (**f**), Co (**g**) elemental mapping of Co_3O_4/CNTs, insets: a photograph of a microdasys cactus, enlarged HRTEM images.

$$2CoOOH + Co(OH)_2 \rightarrow Co_3O_4\downarrow + 2H_2O \quad (5)$$

However, the as prepared Co_3O_4/CNTs were found with a highly crystalline form. The growth of Co_3O_4 nanocactus grown on CNTs (Figure S1) was confirmed by transmission electron microscopy (TEM) analysis in Fig. 2. TEM revealed that the numerous nano-sized Co_3O_4 cactus were grown onto CNTs (Fig. 2a) and the average size of a single unit of nanocactus was ~25 nm in length with ~5 nm thick sidewall (Fig. 2b). High resolution TEM (HRTEM) showed the crystalline spinel structure of the Co_3O_4 nanocactus (Fig. 2c) and the lattice spacing of 2.4 Å and 2.8 Å can be assigned to the (311) and (220) planes of typical Co_3O_4[47]. The bulk elemental component of Co_3O_4/CNTs was investigated by energy dispersive X-ray spectroscopy (EDX) in Fig. 2d. The C peak at 0.2 keV was accompanied by an O peak in the EDX spectra. Three Co peaks at ~0.77, 6.9 and 7.63 keV corresponding to $CoL_{\alpha 1}$, $CoL_{\beta 1}$ and $CoL_{\gamma 1}$, respectively, were also obtained in the EDX spectra. The as-prepared Co_3O_4/CNTs consisted of 6.93 wt% Co, 81.93 wt% C, and 11.14 wt% O. Also, Fig. 2 shows bright-fiend TEM image (e) and C (f), Co (g) elemental mapping of Co_3O_4/CNTs sample which confirming once again the presence of C and Co elements.

The TEM results are consistent with the X-ray diffraction (XRD) data. XRD was performed to investigate the phase structure of Co_3O_4/CNTs. In Fig. 3a, several peaks of the pristine Co_3O_4 were consistent with the standard Co_3O_4 (ICDD: 98-008-8940, red line). Except for the broad peak (002) at ~25°, which may be ascribed to disordered stacked graphitic structure of CNTs, the major diffraction peaks of Co_3O_4/CNTs were in good agreement with those of Co_3O_4[48–50]. The type IV N_2 adsorption/desorption isotherm curve with a distinct hysteresis loop in the relative pressure range of 0.45–0.99 confirmed the presence of mesopores in Co_3O_4/CNTs and bare CNTs samples (Fig. 3b). The Brunaue–Emmett–Teller specific surface area (SSA) for Co_3O_4/CNTs was measured to be 373 $m^2 g^{-1}$, which was approximately 3-magnitudes higher than the corresponding typical values for Co_3O_4-decorated carbon nanomaterials (i.e., Co_3O_4/N-rGO, 103.9 $m^2 g^{-1}$; Co@Co_3O_4/NC–1, 111 $m^2 g^{-1}$; Co_3O_4/CNW-A, 166 $m^2 g^{-1}$)[28,30,32]. On the contrary, the SSA for bare CNTs was 133.2 $m^2 g^{-1}$. Barrett–Joyner–Halenda pore size distribution curves confirm the presence of the main mesopores with various sizes between 3 nm and 25 nm (average pore diameter, 6.9 nm) and a pore volume of 1.32 $cm^3 g^{-1}$. The average pore diameter and pore volume were much higher than those of bare CNTs (Fig. 3b inset). Therefore, a large SSA, high pore volume, and wide pore size distribution are the clear indication of facile electrocatalysis on Co_3O_4/CNTs sample.

X-ray photoelectron spectroscopy (XPS) was performed to elucidate the chemical changes and confirmed the cobalt state during Co_3O_4 growth on CNTs. The peaks obtained in the XPS spectra at 284.2, 531.0 and 780.7 eV (Fig. 3c) could be ascribed to C1s, O1s and Co2p, respectively, due to the existence of carbon, oxygen and cobalt

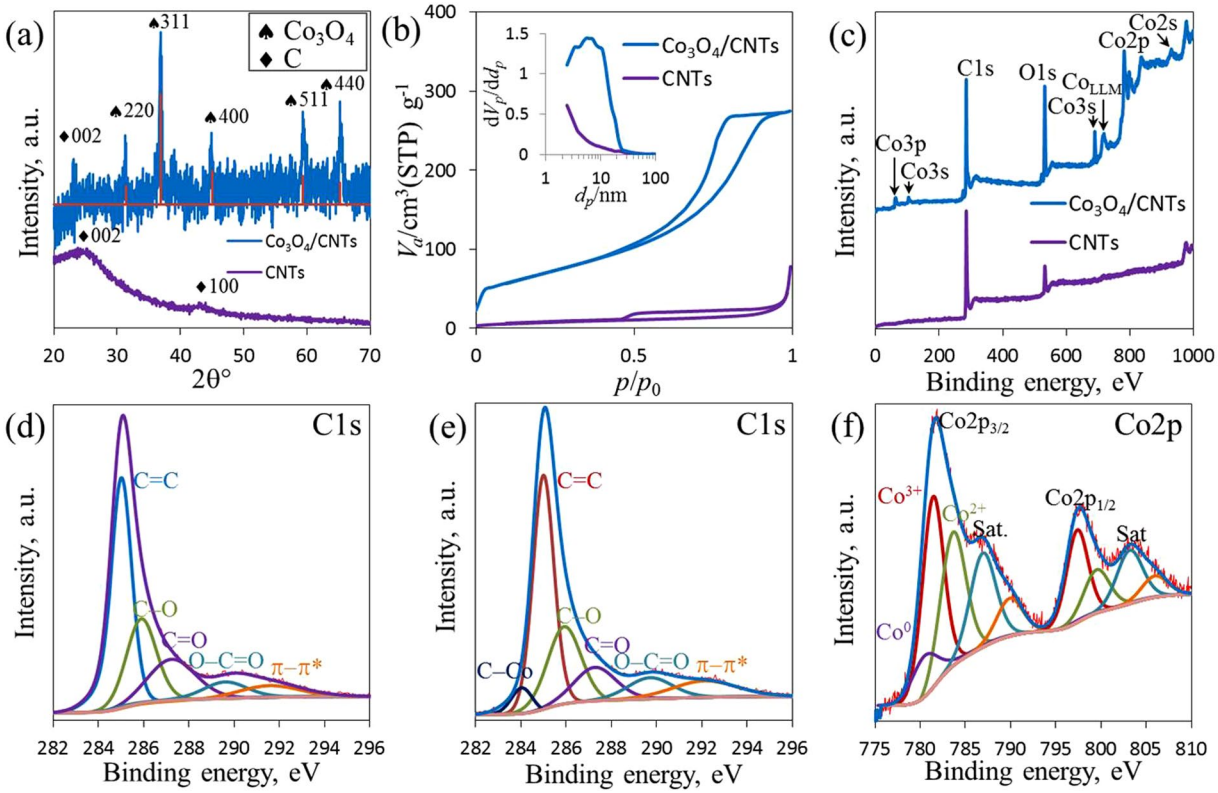

Figure 3. The XRD spectra (**a**), the nitrogen adsorption–desorption isotherms (**b**), XPS spectra (**c**), core level of C1s (**d** and **e**), and Co2p XPS spectrum (**f**) of CNTs and Co_3O_4/CNTs; inset: the corresponding pore-size distribution (**b**).

in Co_3O_4/CNTs. Significant difference was observed in the presence of Co_3O_4 in Co_3O_4/CNTs compared with bare CNTs. The high-resolution C1s XPS spectra of bare CNTs (Fig. 3d) and Co_3O_4/CNTs (Fig. 3e) represent the defective sp^3-carbon and basal-plane sp^2-carbon of CNTs[51]. Both figures showed four absorbance peaks for oxygenated sp^3-carbon at 285.8, 287.3, and 289.7 eV, which were attributed to C–O, C=O, and O–C=O, respectively, including distinct oxygen-free sp^2-carbon (C=C) at 285.0 eV[52]. Moreover, a tiny shakeup peak was obtained at 292.2 eV for π–π*, signifying higher degree of graphitization[53,54]. The tiny peak at low binding energy of 284.1 eV could probably be attributed to the C–Co bond in Co_3O_4/CNTs[55]. The overall elemental composition of Co_3O_4/CNTs is listed in Table S1. Furthermore, XPS confirmed the oxidized state of the Co-species with the detection of binding energies of 781.7 eV and 797.6 eV which were attributed to $Co2p_{3/2}$ and $Co2p_{1/2}$ peaks, respectively (Fig. 3f)[56,57]. However, the Co^0, Co^{3+} and Co^{2+} species were detected at 781.4, 781.6, and 783.8 eV in $Co2p_{3/2}$ with corresponding satellite peak (786.7 eV) due to the presence of Co_3O_4 in the Co_3O_4/CNTs sample. At $Co2p_{1/2}$, the Co^{3+} and Co^{2+} species also appeared at 797.45 eV and 799.6 eV with its shakeup satellite at 803.3 eV. Moreover, the numerical analysis of XPS data was also recorded, and Co was detected as 6.94 wt% with a good ratio of Co^{3+}/Co^{2+} (1.1) at pH 10 which was the lowest value among all pHs (Figure S2 and Table S2).

Electrochemical ORR on Co_3O_4/CNTs. The linear sweep voltammogram (LSV) curves on rotating disk electrode (RDE) exhibited ORR for Co_3O_4/CNTs, bare CNTs (catalyst mass loading, 153 μg cm^{-2}) and 20 wt% Pt/C electrodes in O_2-saturated 0.1 M KOH solution at a scan rate of 5 mV s^{-1} and at 1600 rpm (Fig. 4a) and signify the electrocatalytic ORR performance on all electrodes. The superior electrocatalytic ORR was observed on Co_3O_4/CNTs in terms of the improved onset potential (E_{onset}) of 0.93 V and a half-wave potential ($E_{1/2}$) of 0.83 V than the CNTs (E_{onset}, 0.83 V and $E_{1/2}$, 0.76 V (Figure S3). These values were also superior to those of commercially available Pt/C (E_{onset} of 0.91 V and $E_{1/2}$ of 0.83 V) and several other reported Co_3O_4-based catalysts for ORR[26,58]. Moreover, the current density (j, normalized by electrode area, 0.196 cm^2) at the Co_3O_4/CNTs electrode was higher than that of the CNTs modified electrode and closer to that of Pt/C. Thus, the Co_3O_4/CNTs showed better electrocatalytic activity for ORR in terms of E_{onset}, $E_{1/2}$, and j. This result highlights the importance of the incorporation of nanocactus-shaped Co_3O_4 with CNTs that have mesoporous structure and higher SSA. The ORR dynamics at the Co_3O_4/CNTs electrode were then investigated by RDE, and the results are shown in Fig. 4b. Figure 4b displays a series of RDE curves for ORR using the Co_3O_4/CNTs catalyst at various rotation speeds in same electrolyte at 5 mV s^{-1} scan rate. The obtained data were analyzed using Koutecky–Levich (K—L) equation as follows[58–60]:

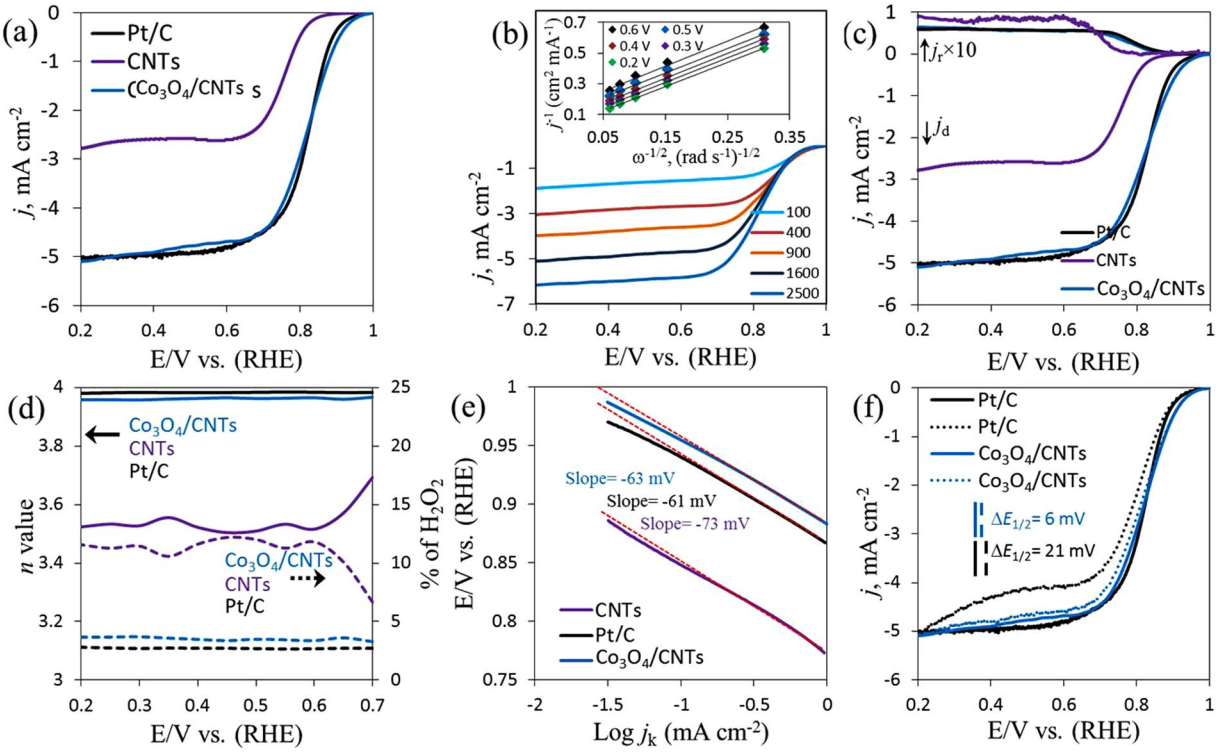

Figure 4. LSV curves for ORR on CNTs, Co_3O_4/CNTs and Pt/C catalyst in O_2-saturated 0.1 M KOH solution at a scan rate of 5 mV s^{-1} and at a rotating speed of 1600 rpm (**a**), LSV curves on Co_3O_4/CNTs in same electrolyte at various rotating speeds and K–L plots in inset (**b**), RRDE curves for ORR at 1600 rpm with a constant applied potential of 0.8 V vs. RHE on the ring electrode (**c**), the transferred electron number and the corresponding H_2O_2 synthesis during ORR (**d**), Tafel plots (**e**) on CNTs, Co_3O_4/CNTs and Pt/C electrodes, and LSV curves on Co_3O_4/CNTs and Pt/C before (solid lines) and after (dotted lines) 3000 cycles (**f**).

$$\frac{1}{j} = \frac{1}{j_k} + \frac{1}{j_L} \tag{6}$$

$$jL = B\omega^{1/2} = 0.62nFAD_{O_2}^{2/3}C_{O_2}\nu^{-1/6}\omega^{1/2} \tag{7}$$

$$j_k = nFkC_{O_2} \tag{8}$$

where j, j_k, and j_L are the measured, kinetic, and diffusion limiting current densities (mA cm^{-2}), respectively; n is the electron transfer number per O_2, and A is the surface area of the working electrode, Moreover, F and T are Faraday constant (96485.3 C mol^{-1}) and temperature, respectively; D_{O_2} and C_{O_2} are the oxygen diffusion coefficient (1.9×10^{-5} cm^2 s^{-1}) and the bulk concentration (1.2 mM L^{-1}), respectively, in 0.1 M KOH[60]; ν is the kinetic viscosity of the electrolyte (1×10^{-2} cm^2 s^{-1}); ω is the angular velocity of electrode (2π*rpm), and k is the electron-transfer rate constant. Based on the K–L equation, a plot of j_k^{-1} vs. $\omega^{-1/2}$ was yield a straight line and the slopes of those plots reflect the B factor in equation (7).

However, Fig. 4b inset shows the K–L plots for Co_3O_4/CNTs electrode and the slopes of all K–L plots remain approximately constant over the studied potential range. This result indicates the number of electrons transferred in the ORR remained constant. Based on equations (6) and (7), the average n value in ORR was estimated to be 4, suggesting a four-electron ($4e^-$) pathway for electrocatalytic ORR[61–63]. The ORR dynamics on the CNTs electrode were also investigated by RDE and the average n value in ORR was estimated to be 3.6 from corresponding K–L plots (Figure S4). The j_k obtained from the intercept of the K–L plots for the Co_3O_4/CNTs (16.5 mA cm^{-2} at 0.8 V) was 3.1-magnitudes larger than that of bare CNTs (5.2 mA cm^{-2}) catalyst and similar to that of Pt/C (17.3 mA cm^{-2}). The ORR activities on as-synthesized Co_3O_4/CNTs at various pH values were also investigated (Figure S5a). Although the Co_3O_4/CNTs @ pH 12 has the highest Co_3O_4 (Table S2), the relatively low Co^{3+}/Co^{2+} might lead to a high charge-transfer (Figure S5b). Hence, a relatively better electrocatalytic activity was observed at Co_3O_4/CNTs @ pH 10 in based on the higher j_k among all pH-dependent Co_3O_4/CNTs (Figure S5a inset).

The rotating ring–disk electrode (RRDE) measurement was performed to further evaluate the ORR pathway on Co_3O_4/CNTs, bare CNTs, and Pt/C electrodes. The Co_3O_4/CNTs electrode exhibited high disk current density (j_d) for ORR and much lower ring current density (j_r) than CNTs. The j_r profiles accompanied with further

reduction of peroxide species synthesized during ORR process are shown in the upper curves. Both j_d and j_r from Pt/C are very similar to that of Co_3O_4/CNTs.

The RRDE data were used to further verify the transferred electron number and monitor the corresponding H_2O_2 formation on aforementioned three electrodes during ORR process from equations (9) and (10)[28,64] in Fig. 4d. The average n value for ORR at the Co_3O_4/CNTs electrode (3.96) was consistently higher than that at the CNTs (3.6) over the tested potential range of 0.7–0.2 V (vs. RHE). The corresponding H_2O_2 yields were 3.5% and 9.6% for Co_3O_4/CNTs and CNTs, respectively, over the same potential range. The calculated n value (3.98) and H_2O_2 (2.9%) yield on Pt/C were slightly higher than the Co_3O_4/CNTs. The calculated n values are similar to the result obtained from the K–L plots, signifying that the ORR on Co_3O_4/CNTs hybrid was mainly by $4e^-$ involved pathway and the main byproduct was H_2O.

$$n = \frac{4i_d}{i_d + \frac{i_r}{N}} \tag{9}$$

$$H_2O_2\% = \frac{200\frac{i_r}{N}}{i_d + \frac{i_r}{N}} \tag{10}$$

$$N = \frac{-i_r}{i_d} \tag{11}$$

where N is the collection efficiency of the RRDE (0.37), and i_d and i_r are the disk and ring electrode currents, respectively.

The estimated j_k values were plotted against the electrode potential to investigate the Tafel behavior of Co_3O_4/CNTs, CNTs and Pt/C (Fig. 4e). The better ORR activity on Co_3O_4/CNTs was further confirmed by the lower Tafel slope of 63 mV dec^{-1} at low overpotential (η) than the CNTs (73 mV dec^{-1}) and similar to that of Pt/C (61 mV dec^{-1}). Furthermore, the LSV curves before and after the accelerated degradation test (ADT) on Co_3O_4/CNTs and Pt/C in Fig. 4f. It was found that the $E_{1/2}$ shifted largely at the negative direction (21 mV), and j_L lost 17.9% on Pt/C after 3000 consecutive cycles. By contrast, the 3.5- and 9-magnitudes lower $E_{1/2}$ shift (6 mV) and j_L loss (2%) were observed on the Co_3O_4/CNTs under the same conditions. Moreover, Figure S6a shows the current density as the function of time by chronoamperometry technique for Co_3O_4/CNTs and Pt/C at an applied potential of 0.8 V. The j was maintained up to 93% after 20 h run in real condition, indicating that the catalytic activity on Co_3O_4/CNTs could be sustained for a long time. For Pt/C, the catalytic activity was then maintained up to 76% with the same period of time. In addition, the Co_3O_4/CNTs electrode demonstrated good methanol tolerance than the Pt/C (Figure S6b). The TEM image of used Co_3O_4/CNTs displays the decay morphology with the crystalline nature of Co_3O_4 after 20 h of real-time continuous monitoring. These results indicate that the Co_3O_4/CNTs are a competent ORR electrocatalyst because of its better electrocatalytic activity, fuel selectivity, and operational stability than the Pt/C.

Electrochemical OER on Co_3O_4/CNTs. To evaluate the potential use of our hybrid catalyst, we employed Co_3O_4/CNTs electrode to evaluate the electrocatalytic OER. The OER catalytic activities of all catalysts were studied by LSV at 5 mV s^{-1}. The Co_3O_4/CNTs were used with same mass loading and afforded higher OER activity than either bare bulk Co_3O_4, CNTs or RuO_2 in Fig. 5. Figure 5a shows that the E_{onset} for bulk Co_3O_4 was 1.55 V and the maximum j was 13.6 mA cm^{-2} at 1.7 V. The E_{onset} for RuO_2 was 1.36 V with maximum of $j = 31$ mA cm^{-2} at the same electrode potential. However, considerable negative shifted in the E_{onset} was observed at Co_3O_4/CNTs (1.43 V) with highest $j = 70.8$ mA cm^{-2} at 1.7 V and the CNTs showed the lowest performance than all electrodes. However, the Co_3O_4/CNTs electrode showed a potential of 1.55 V at the current density of 10 mA cm^{-2} $\left(E_{j_{10}}\right)$, which was lower than that of bulk Co_3O_4 (1.68 V) and RuO_2 (1.61 V). Moreover, as shown in Fig. 5a inset, the η required to drive a j_{10} for the Co_3O_4/CNTs was 280 mV, which was also significantly lower than that for the bulk Co_3O_4 and RuO_2 (440 mV and 380 mV, respectively). Thus, the Co_3O_4/CNTs exhibited higher OER activity than the bulk Co_3O_4, CNTs and RuO_2 electrodes in respect to the η and j. This result indicating that the Co_3O_4/CNTs have higher density of active sites than bulk Co_3O_4 and CNTs, and the porous Co_3O_4 served as the better active catalytic site for the superior OER even better than benchmark RuO_2 which resulted in the synergic effect of Co_3O_4 and CNTs, the porous nanocactus-like structure, and better Co^{3+}/Co^{2+} ratio. These characteristics allowed improved ability for electron transfer. The poor current densities of bare CNTs and Co_3O_4 were probably due to the degradation nature of carbon[32] and aggregation with less conducive nature, respectively[26].

The Tafel slope of each catalyst beyond the E_{onset} was calculated to understand in detail the OER mechanism and the result are shown Fig. 5b. Tafel plots display a lower Tafel slope of 64 mV dec^{-1} for Co_3O_4/CNTs than those of RuO_2 (71 mV dec^{-1}), bulk Co_3O_4 (73 mV dec^{-1}) and CNTs (98 mV dec^{-1}), indicating more favorable kinetics toward OER on the Co_3O_4/CNTs electrode[32,65]. The Tafel slope of Co_3O_4/CNTs was also comparable to other reported Co_3O_4-based OER catalysts[26,66]. The OER mechanism can be assumed as follows according to the Tafel slope of Co_3O_4/CNTs. The OER on active Co−O-system[65] in Co_3O_4/CNTs catalyst was initiated by water adsorption and the formation of adsorbed (ads) reactive intermediate, OH^*_{abs}, by releasing a proton and electron in equation (12). Afterwards, this OH^*_{abs} was converted to another type OH, OH^*_{abs}, in equation (13) (both OH are chemically same but energetically different). In equation (14), a second proton and electron transfer yielded an oxide intermediate, and this step is a rate-determining step (RDS). Recombination of two oxide intermediates completed one reaction turnover in equation (15)[67].

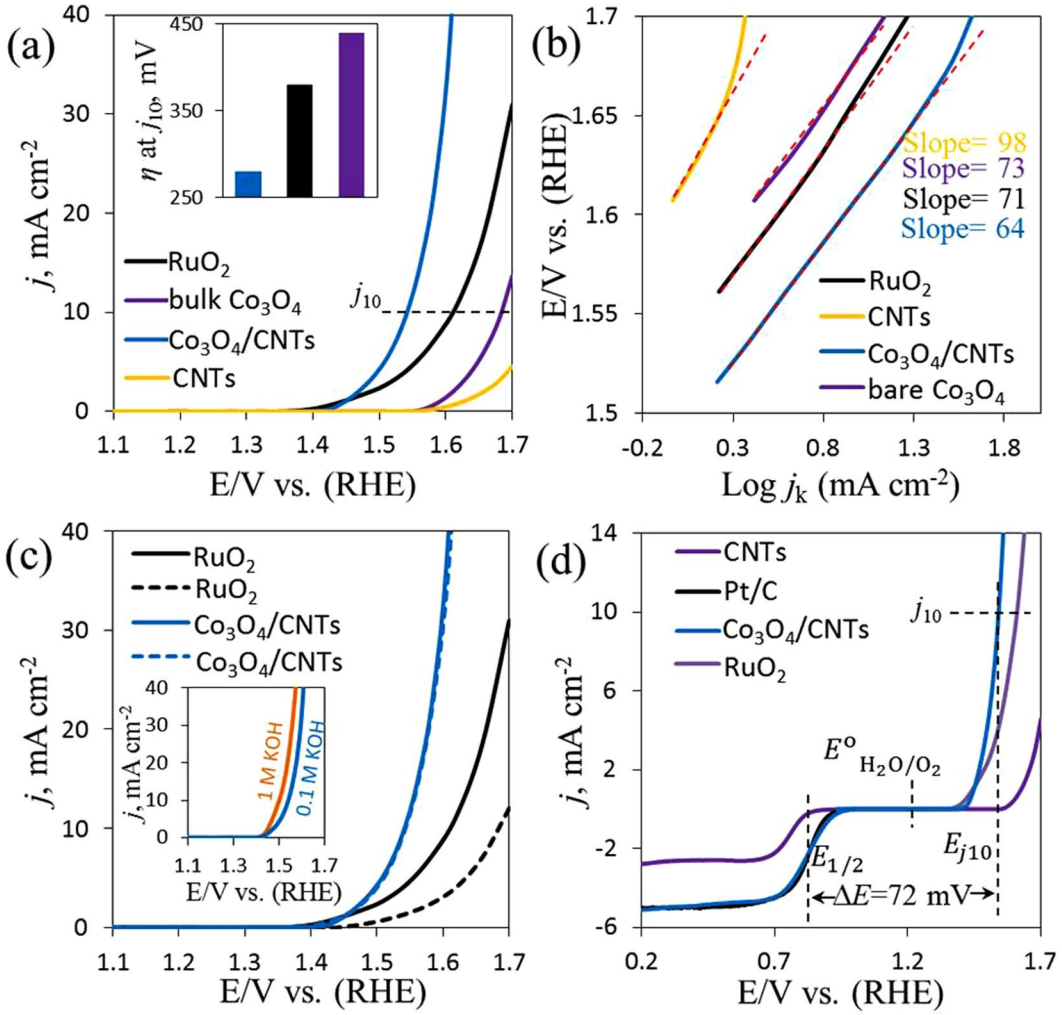

Figure 5. Comparison of the OER activity of CNTs, bulk Co_3O_4, Co_3O_4/CNTs and RuO_2 electrodes by LSV (**a**), corresponding Tafel plots of those electrodes (**b**), LSV curves for the 1st and 1000th potential cycles (**c**), bifunctional catalytic activities of CNTs, Co_3O_4/CNTs and benchmarks Pt/C or RuO_2 catalysts toward both ORR and OER (**d**); the overall LSV curves in the potential range of 0.2 to 1.7 V was investigated in argon-saturated 0.1 M KOH solution at 5 mV s^{-1} scan rate and at the rotating speed of 1600 rpm. Insets: the comparison of overpotential at j_{10} (**a**) and OER activity of Co_3O_4/CNTs in argon-saturated 0.1 and 1 M KOH solution (**c**).

$$Co–O + H_2O \rightarrow O–Co–OH^{*}_{abs} + H^{+} + e^{-} \quad (12)$$

$$O–Co–OH^{*}_{abs} \rightarrow O–Co-OH_{abs} \quad (13)$$

$$O–Co–OH_{abs} \xrightarrow{RDS} O–Co–O_{abs} + H^{+} + e^{-} \quad (14)$$

$$O–Co–O_{abs} + O–Co–O_{abs} \rightarrow 2Co–O + O_2\uparrow \quad (15)$$

Furthermore, the electrochemical stability of Co_3O_4/CNTs electrode was also compared with RuO_2 under a fixed η and electrolyte conditions. Good stability of Co_3O_4/CNTs electrode was confirmed by the similar LSV curves measured at the 1st and 1000th potential cycles (Fig. 5c). The used catalyst was characterized by XPS, and the results suggest that amperometric operation did not change significantly in the chemical states except the increase in C–O bond in CNTs and satellite band in cobalt (Figure S7). These results also suggest that Co_3O_4/CNTs have longer stability in electrochemical process than the RuO_2. The OER processes at Co_3O_4/CNTs electrode in 0.1 and 1 M KOH exhibit the same E_{onset} of 1.43 V (Fig. 5c inset). At higher potentials, the more rapid increase in current density was observed for 1 M KOH owing to higher conductivity of the electrolyte. At 270 mV overpotential, $j = 22$ mA cm^{-2} was obtained in 1 M KOH solution, while it was 10 mA cm^{-2} in 0.1 M KOH.

Name	Electrolyte	$E_{1/2}$ (V vs. RHE)	$E_{j_{10}}$ (V vs. RHE)	ΔE (V)	References
Co_3O_4/CNTs	0.1 M KOH	0.83	1.55	0.72	This work
Co-N/G-600	0.1 M KOH	0.764*	1.724*	0.96	[21]
Co_3O_4/N-rmGO	0.1 M KOH	0.83	1.54	0.71	[26]
Co_3O_4/NPC	0.1 M KOH	0.74*	1.63*	0.89	[28]
Co@Co_3O_4/NC-1	0.1 M KOH	0.80	1.65	0.85	[30]
Co_3O_4/CNW-B	0.1 M KOH	0.755*	1.556*	0.801	[37]
Co_3O_4/N-GAs	0.1 M KOH	0.87	1.66	0.79	[66]
CMO/N-rGO	0.1 M KOH	0.80	1.66	0.86	[69]
Co_9S_8(600)/N,S-GO	0.1 M KOH	0.75	1.63	0.88	[70]
Co_xO_y/NC	0.1 M KOH	0.80	1.66	0.86	[71]

Table 1. The bifunctional catalytic activity of Co_3O_4/CNTs catalyst for ORR and OER. *Converted V vs. RHE.

The overall oxygen activity of the Co_3O_4/CNTs as a bifunctional catalyst could be evaluated (Fig. 5d) by the potential difference (ΔE) between the $E_{j_{10}}$ for OER and $E_{1/2}$ for ORR[68]. However, the Co_3O_4/CNTs catalyst showed the smallest ΔE of 0.72 V and this value was markedly lower than the ΔE obtained using commercial Pt/C (0.85 V) and many other Co- and Co_3O_4-based materials i.e., Co-N/G-600, 0.96 V; Co@Co_3O_4/NC-1, 0.85 V; Co_3O_4/N-Gas, 0.79 V[21,30,67]. This result signifies better reversible oxygen electrode. The detailed comparison with various Co- and Co_3O_4-based materials is shown in Table 1. These results clearly indicate that the Co_3O_4/CNTs catalyst is a promising low-cost and efficient catalyst for both ORR and OER.

Conclusion

We demonstrated an easy and generic method to synthesize a unique nanocactus-like structure of Co_3O_4 material embedded onto CNTs for bifunctional electrocatalysis. The newly developed Co_3O_4/CNTs were an effective bifunctional ORR and OER electrocatalyst with comparatively better activities and stability than the Pt/C or RuO_2 because of their unique architecture with large surface area, rich active sites, and good electron transfer properties. The excellent catalysis and stability of Co_3O_4/CNTs with abundant active sites could be attributed to the strong interaction between the nanocactus-shaped Co_3O_4 and CNTs. Thus, Co_3O_4/CNTs are promising alternatives to noble metal-based catalysts for FCs and water splitting applications because of their low-cost, facile synthesis, and excellent catalysis and stability.

References

1. Dai, L., Xue, Y., Qu, L., Choi, H.-J. & Baek, J.-B. Metal-free catalysts for oxygen reduction reaction. *Chem. Rev.* **115**, 4823–4892 (2015).
2. Ahmed, M. S., Jeong, H., You, J.-M. & Jeon, S. Electrocatalytic reduction of dioxygen at a modified glassy carbon electrode based on Nafion-dispersed single-walled carbon nanotubes and cobalt–porphyrin with palladium nanoparticles in acidic media. *Electrochim. Acta* **56**, 4924–4929 (2011).
3. Boyd, A., Dube, I., Fedorov, G., Paranjape, M. & Barbara, P. Gas sensing mechanism of carbon nanotubes: From single tubes to high-density networks. *Carbon* **69**, 417–423 (2014).
4. Begum, H., Ahmed, M. S. & Jeon, S. A novel δ-MnO_2 with carbon nanotubes nanocomposite as an enzyme-free sensor for hydrogen peroxide electrosensing. *RSC Adv.* **6**, 50572–50580 (2016).
5. Li, L. *et al.* Chemical strategies for enhancing activity and charge transfer in ultrathin Pt nanowires immobilized onto nanotube supports for the oxygen reduction reaction. *ACS Appl. Mater. Interfaces* **8**, 34280–34294 (2016).
6. Hu, C. *et al.* Newly-designed complex ternary Pt/PdCu nanoboxes anchored on three-dimensional graphene framework for highly efficient ethanol oxidation. *Adv. Mater.* **24**, 5493–5498 (2012).
7. Gong, K., Du, F., Xia, Z., Durstock, M. & Dai, L. Nitrogen-doped carbon nanotube arrays with high electrocatalytic activity for oxygen reduction. *Science* **323**, 760–764 (2009).
8. Jiao, L., Zhou, Y.-X. & Jiang, H.-L. Metal–organic framework-based CoP/reduced graphene oxide: high-performance bifunctional electrocatalyst for overall water splitting. *Chem. Sci.* **7**, 1690–1695 (2016).
9. Begum, H., Ahmed, M. S. & Jeon, S. Highly efficient dual active palladium nanonetwork electrocatalyst for ethanol oxidation and hydrogen evolution. *ACS Appl. Mater. Interfaces* 9, (39303–39311 (2017).
10. Shui, J., Wang, M., Du, F. & Dai, L. N-doped carbon nanomaterials are durable catalysts for oxygen reduction reaction in acidic fuel cells. *Sci. Adv.* **1**, e1400129 (2015).
11. Wang, H. *et al.* Bifunctional non-noble metal oxide nanoparticle electrocatalysts through lithium-induced conversion for overall water splitting. *Nat. Commun.* **6**, 7261 (2015).
12. Wang, J. *et al.* Recent progress in cobalt-based heterogeneous catalysts for electrochemical water splitting. *Adv. Mater.* **28**, 215–230 (2016).
13. Ahmed, M. S., Park, D. & Jeon, S. Ultrasmall $Pd_mMn_{1-m}O_x$ binary alloyed nanoparticles on graphene catalysts for ethanol oxidation in alkaline media. *J. Power Sources* **308**, 180–188 (2016).
14. Lim, B. *et al.* Pd-Pt bimetallic nanodendrites with high activity for oxygen reduction. *Science* **324**, 1302–1305 (2009).
15. Choe, J. E., Ahmed, M. S. & Jeon, S. 3,4-ethylenedioxythiophene functionalized graphene with palladium nanoparticles for enhanced electrocatalytic oxygen reduction reaction. *J. Power Sources* **281**, 211–218 (2015).
16. Begum, H., Ahmed, M. S. & Jeon, S. Simultaneous reduction and nitrogen functionalization of graphene oxide using lemon for metal-free oxygen reduction reaction. *J. Power Sources* **372**, 116–124 (2017).
17. Shao, Y., Liu, J., Wang, Y. & Lin, Y. Novel catalyst support materials for PEM fuel cells: current status and future prospects. *J. Mater. Chem.* **19**, 46–59 (2009).
18. Ahmed, M. S. & Jeon, S. Highly active graphene-supported Ni_xPd_{100-x} binary alloyed catalysts for electro-oxidation of ethanol in an alkaline media. *ACS Catal.* **4**, 1830–1837 (2014).
19. Joo, Y., Ahmed, M. S., Han, H. S. & Jeon, S. Preparation of electrochemically reduced graphene oxide-based silver-cobalt alloy nanocatalysts for efficient oxygen reduction reaction. *Int. J. Hydrogen Energy* **42**, 21751–21761 (2017).

20. Tian, J., Liu, Q., Cheng, N., Asiri, A. M. & Sun, X. Self-supported Cu_3P nanowire arrays as an integrated high-performance three-dimensional cathode for generating hydrogen from water. *Angew. Chem. Int. Ed.* **53**, 9577–9581 (2014).
21. Wang, Q., Hu, W. & Huang, Y. Nitrogen doped graphene anchored cobalt oxides efficiently bi-functionally catalyze both oxygen reduction reaction and oxygen revolution reaction. *Int. J. Hydrogen Energy* **42**, 5899–5907 (2017).
22. Laursen, A. B. *et al*. Nanocrystalline Ni_5P_4: a hydrogen evolution electrocatalyst of exceptional efficiency in both alkaline and acidic media. *Energy Environ. Sci.* **8**, 1027–1034 (2015).
23. Tüysüz, H., Hwang, Y. J., Khan, S. B., Asiri, A. M. & Yang, P. Mesoporous Co_3O_4 as an electrocatalyst for water oxidation. *Nano Res.* **6**, 47–54 (2013).
24. Li, G. *et al*. Design of ultralong single-crystal nanowire-based bifunctional electrodes for efficient oxygen and hydrogen evolution in a mild alkaline electrolyte. *J. Mater. Chem. A* **5**, 10895–10901 (2017).
25. Abidat, I. *et al*. Electrochemically Induced Surface Modifications of Mesoporous Spinels (Co_3O_4-δ, $Mnco_2o_4$-δ, $Nico_2o_4$-δ) as the origin of the OER activity and stability in alkaline medium. *J. Mater. Chem. A* **3**, 17433–17444 (2015).
26. Liang, Y. *et al*. Co_3O_4 nanocrystals on graphene as a synergistic catalyst for oxygen reduction reaction. *Nat. Mater.* **10**, 780–786 (2011).
27. Liu, Y., Jiang, H., Zhu, Y., Yang, X. & Li, C. Transition metals (Fe, Co, And Ni) encapsulated in nitrogen-doped carbon nanotubes as bi-functional catalysts for oxygen electrode reactions. *J. Mater. Chem. A* **4**, 1694–1701 (2016).
28. Huang, Y., Zhang, M., Liu, P., Cheng, F. & Wang, L. Co_3O_4 supported on N, P-doped carbon as a bifunctional electrocatalyst for oxygen reduction and evolution reactions. *Chinese J. Catal.* **37**, 1249–1256 (2016).
29. Grewe, T., Deng, X., Weidenthaler, C., Schuth, F. & Tuysuz, H. Design of ordered mesoporous composite materials and their electrocatalytic activities for water oxidation. *Chem. Mater.* **25**, 4926–4935 (2013).
30. Aijaz, A. *et al*. $Co@Co_3O_4$ encapsulated in carbon nanotube-grafted nitrogen-doped carbon polyhedra as an advanced bifunctional oxygen electrode. *Angew. Chem. Int. Ed.* **55**, 4087–4091 (2016).
31. Xu, L. *et al*. Plasma-engraved Co_3O_4 nanosheets with oxygen vacancies and high surface area for the oxygen evolution reaction. *Angew. Chem. Int. Ed.* **55**, 5277–5281 (2016).
32. Liu, S., Li, L., Ahn, H. S. & Manthiram, A. Delineating the roles of Co_3O_4 and N-doped carbon nanoweb (CNW) in bifunctional Co_3O_4/CNW catalysts for oxygen reduction and oxygen evolution reactions. *J. Mater. Chem. A* **3**, 11615–11623 (2015).
33. Yeo, B. S. & Bell, A. T. Enhanced activity of gold-supported cobalt oxide for the electrochemical evolution of oxygen. *J. Am. Chem. Soc.* **133**, 5587–5593 (2011).
34. Nguyen, T. T. *et al*. Facile synthesis of cobalt oxide/reduced graphene oxide composites for electrochemical capacitor and sensor applications. *Solid State Sci.* **53**, 71–77 (2016).
35. Zhang, Y. *et al*. Crystal plane-dependent electrocatalytic activity of Co_3O_4 toward oxygen evolution reaction. *Catal. Commun.* **67**, 78–82 (2015).
36. Begum, H., Ahmed, M. S. & Jeon, S. Ultra-fast and highly sensitive enzyme-free glucose biosensing on a nickel–nickel oxide core–shell electrode. *RSC Adv.* **7**, 3554–3562 (2017).
37. Fan, T., Yin, F., Wang, H., He, X. & Li, G. A metaleorganic-framework/carbon composite with enhanced bifunctional electrocatalytic activities towards oxygen reduction/evolution reactions. *Int. J. Hydrogen Energy* **42**, 17376–17385 (2017).
38. Lu, H., Huang, Y., Yan, J., Fan, W. & Liu, T. Nitrogen-doped graphene/carbon nanotube/Co_3O_4 hybrids: one-step synthesis and superior electrocatalytic activity for the oxygen reduction reaction. *RSC Adv.* **5**, 94615–94622 (2015).
39. Xu, N. *et al*. Self-assembly formation of bi-functional Co_3O_4/MnO_2-CNTs hybrid catalysts for achieving both high energy/power density and cyclic ability of rechargeable zinc-air battery. *Sci. Rep.* **6**, 33590 (2016).
40. Li, X. *et al*. 3D hollow sphere Co_3O_4/MnO_2-*CNTs: its high-performance* bi-functional cathode catalysis and application in rechargeable zinc-air battery. *Green Energy & Environ.* **2**, 316–328 (2017).
41. Hong, W., Shang, C., Wang, J. & Wang, E. Bimetallic PdPt nanowire networks with enhanced electrocatalytic activity for ethylene glycol and glycerol oxidation. *Energy Environ. Sci.* **8**, 2910–2915 (2015).
42. Begum, H., Ahmed, M. S. & Jeon, S. Electrodeposited palladium nanotubes on nanoclusters mosaic basement for electrooxidation of hydrazine. *J. Nanosci. Nanotechnol.* **17**, 4961–4969 (2017).
43. Hu, C. & Dai, L. Multifunctional carbon-based metal-free electrocatalysts for simultaneous oxygen reduction, oxygen evolution, and hydrogen evolution. *Adv. Mater.* **29**, 1604942 (2017).
44. Kim, H. *et al*. Coordination tuning of cobalt phosphates towards efficient water oxidation catalyst. *Nat. Commun.* **6**, 8253 (2015).
45. Ahmed, M. S. & Jeon, S. Electrochemical activity evaluation of chemically damaged carbon nanotube with palladium nanoparticles for ethanol oxidation. *J. Power Sources* **282**, 479–488 (2015).
46. Hussain, M. M., Rahman, M. M., Asiriab, A. M. & Awual, M. R. Non-enzymatic simultaneous detection of Lglutamic acid and uric acid using mesoporous Co_3O_4 nanosheets. *RSC Adv.* **6**, 80511–80521 (2016).
47. Liu, Q., Xu, J., Changab, Z. & Zhang, X. Direct electrodeposition of cobalt oxide nanosheets on carbon paper as free-standing cathode for Li–O_2 battery. *J. Mater. Chem. A* **2**, 6081–6085 (2014).
48. Ahmed, M. S., Kim, D. & Jeon, S. Covalently grafted platinum nanoparticles to multi walled carbon nanotubes for enhanced electrocatalytic oxygen reduction. *Electrochim. Acta* **92**, 168–175 (2013).
49. Liu, Q. *et al*. Carbon nanotubes decorated with CoP nanocrystals: a highly active non-noble-metal nanohybrid electrocatalyst for hydrogen evolution. *Angew. Chem.* **126**, 6828–6832 (2014).
50. Zhou, X. *et al*. Facile synthesis of a Co_3O_4@carbon nanotubes/polyindole composite and its application in all-solid-state flexible supercapacitors. *J. Mater. Chem. A* **3**, 13011–13015 (2015).
51. Ahmed, M. S., Han, H. S. & Jeon, S. One-step chemical reduction of graphene oxide with oligothiophene for improved electrocatalytic oxygen reduction reactions. *Carbon* **61**, 164–172 (2013).
52. Ahmed, M. S. & Jeon, S. New functionalized graphene sheets for enhanced oxygen reduction as metal-free cathode electrocatalysts. *J. Power Sources* **218**, 168–173 (2012).
53. Tao, L. *et al*. Edge-rich and dopant-free graphene as a highly efficient metal-free electrocatalyst for the oxygen reduction reaction. *Chem. Commun.* **52**, 2764–2767 (2016).
54. Begum, H., Ahmed, M. S. & Jeon, S. New approach for porous chitosan−graphene matrix preparation through enhanced amidation for synergic detection of dopamine and uric acid. *ACS Omega* **2**, 3043–3054 (2017).
55. Deniau, G., Azoulay, L., Jegou, P., Chevallier, G. L. & Palacin, S. Carbon-to-metal bonds: electrochemical reduction of 2-butenenitrile. *Surf. Sci.* **600**, 675–684 (2006).
56. Gao, Y. *et al*. Double metal ions synergistic effect in hierarchical multiple sulfide microflowers for enhanced supercapacitor performance. *ACS Appl. Mater. Interfaces* **7**, 4311–4319 (2015).
57. An, T. *et al*. Co_3O_4 nanoparticles grown on N-doped vulcan carbon as a scalable bifunctional electrocatalyst for rechargeable zinc–air batteries. *RSC Adv.* **5**, 75773–75780 (2015).
58. Xu, J., Gao, P. & Zhao, T. S. Non-precious Co_3O_4 nano-rod electrocatalyst for oxygen reduction reaction in anion-exchange membrane fuel cells. *Energy Environ. Sci.* **5**, 5333–5339 (2012).
59. Ahmed, M. S. & Kim, Y.-B. 3D graphene preparation via covalent amide functionalization for efficient metal-free electrocatalysis in oxygen reduction. *Sci. Rep.* **7**, 43279 (2017).
60. Wang, S., Yu, D., Dai, L., Chang, D. W. & Baek, J.-B. Polyelectrolyte-functionalized graphene as metal-free electrocatalysts for oxygen reduction. *ACS Nano* **8**, 6202–6209 (2011).

61. Ahmed, M. S. & Kim, Y.-B. Amide-functionalized graphene with 1,4-diaminobutane as efficient metal-free and porous electrocatalyst for oxygen reduction. *Carbon* **111**, 577–586 (2017).
62. Zheng, Y., Jiao, Y., Ge, L., Jaroniec, M. & Qiao, S. Z. Two-step boron and nitrogen doping in graphene for enhanced synergistic catalysis. *Angew. Chem. Int. Ed.* **52**, 3110–3116 (2013).
63. Park, D., Ahmed, M. S. & Jeon, S. Covalent functionalization of graphene with 1,5- diaminonaphthalene and ultrasmall palladium nanoparticles for electrocatalytic oxygen reduction. *Int. J. Hydrogen Energy* **42**, 2061–2070 (2017).
64. Lee, K., Ahmed, M. S. & Jeon, S. Electrochemical deposition of silver on manganese dioxide coated reduced graphene oxide for enhanced oxygen reduction reaction. *J. Power Sources* **288**, 261–269 (2015).
65. Zhu, J., Ren, X., Liu, J., Zhang, W. & Wen, Z. Unraveling the catalytic mechanism of Co_3O_4 for the oxygen evolution reaction in a $Li-O_2$ battery. *ACS Catal.* **5**, 73–81 (2015).
66. Yu, D., Xu, C., Su, Y., Liu, D. & He, X. Nitrogen-doped graphene aerogels-supported cobaltosic oxide nanocrystals as high-performance bi-functional electrocatalysts for oxygen reduction and evolution reactions. *J. Electroanal. Chem.* **787**, 46–54 (2017).
67. Antolini, E. Iridium as catalyst and cocatalyst for oxygen evolution/reduction in acidic polymer electrolyte membrane electrolyzers and fuel cells. *ACS Catal.* **4**, 1426–1440 (2014).
68. Chen, S. *et al*. Ionic liquid-assisted synthesis of N/S-double doped graphene microwires for oxygen evolution and Zn–air batteries. *Energy Storage Mater.* **1**, 17 (2015).
69. Prabu, M., Ramakrishnan, P. & Shanmugam, S. $CoMn_2O_4$ nanoparticles anchored on nitrogen-doped graphene nanosheets as bifunctional electrocatalyst for rechargeable zinc–air battery. *Electrochem. Commun.* **41**, 59–63 (2014).
70. Ganesan, P., Prabu, M., Sanetuntikul, J. & Shanmugam, S. Cobalt sulfide nanoparticles grown on nitrogen and sulfur codoped graphene oxide: an efficient electrocatalyst for oxygen reduction and evolution reactions. *ACS Catal.* **5**, 3625–3637 (2015).
71. Masa, J. *et al*. Mn_xO_y/NC and Co_xO_y/NC nanoparticles embedded in a nitrogen-doped carbon matrix for high-performance bifunctional oxygen electrodes. *Angew. Chem. Int. Ed.* **53**, 8508–8512 (2014).

Acknowledgements

This work was supported in part by the National Research Foundation of Korea (15H1C1A1035825 and 15R1A4A1041746) and in part by Korea Electric Power Cooperation (KEPCO).

Author Contributions

M.S. Ahmed performed all electrochemical experiments, wrote the manuscript and analyzed all the results with due discussion with B. Choi and Y.B. Kim.

Additional Information

Supplementary information accompanies this paper at https://doi.org/10.1038/s41598-018-20974-1.

Competing Interests: The authors declare no competing interests.

Publisher's note: Springer Nature remains neutral with regard to jurisdictional claims in published maps and institutional affiliations.